What determines the stability of Fe-N-C catalysts in HT-PEMFCs?

Julia Müller-Hülstede [a], Henrike Schmies *[a], Dana Schonvogel [a], Quentin Meyer [b], Yan Nie [b], Chuan Zhao [b], Peter Wagner [a], Michael Wark [c]

[a] Institute of Engineering Thermodynamics, German Aerospace Center (DLR), Carl-von-Ossietzky-Str. 15, 26129, Oldenburg, Germany

[b] School of Chemistry, The University of New South Wales, NSW 2052, Sydney, Australia

[c] Institute of Chemistry, Carl von Ossietzky University, Carl-von-Ossietzky-Str. 9-11, 26129, Oldenburg, Germany

* Corresponding author: henrike.schmies@dlr.de

Abstract

Fe-N-C catalysts are an attractive low-cost alternative to Pt for the oxygen reduction reaction (ORR) in high-temperature proton exchange membrane fuel cells (HT-PEMFCs) as they are less sensitive to phosphate poisoning, but they suffer from poor stability and unclear degradation mechanisms. In this study, the activation and degradation mechanisms of HT-PEMFCs with several classes of Fe-N-Cs operating for 90 h are identified using a combination of operando electrochemical and post-mortem physical analysis. While simultaneous activation in terms of accelerated ORR processes takes place by acid redistribution, the degradation of the catalyst leads to drastic performance loss (-27 %) within the first 24 h. Carbon corrosion has a lower impact and the strongest degradation is attributed to active site deactivation e.g. by transformation to inactive nanoparticles or by site loss. This study helps to understand the degradation of Fe-N-Cs in HT-PEMFC and points to the necessary and inevitable modification of single-atom catalysts.

Keywords

PGM-free catalyst; HT-PEMFC; Stability; Fe-N-C

Highlights

- Voltage decay within first 24 h of HT-PEMFC operation independent of Fe-N-C type
- Stability of Fe-N-C in HT-PEMFC independent of electrochemical characterization in single-cell
- Voltage loss attributed to reactive oxygen species formation and Fe-N_x deactivation
- No positive effect from acid distribution due to degradation of catalyst in beginning of operation

1 Introduction

Proton exchange membrane fuel cell operated at high-temperature around 160 °C (HT-PEMFC) allows for operations with hydrogen or reformate e.g. from green methanol which is beneficial for volume-critical applications.[1] Moreover, their easier heat management compared to the low temperature (LT)-PEMFC technology is attractive for heavy-duty applications.[2] However, Pt-based catalyst applied in HT-PEMFCs suffer from phosphate-induced deactivation at the anode and cathode and requires high electrode loadings of 0.7-1 mg_{Pt} cm^{-2}.[3] Therefore, the investigation of Pt-free catalysts is crucial to increase the viability of HT-PEMFC.

Iron-nitrogen-carbon (Fe-N-C) catalysts, consisting of single metal sites coordinated to nitrogen sites (Fe-N_x) embedded into a partly-graphitized carbon network are the most active Pt-free catalysts for the oxygen reduction reaction (ORR) in acidic electrolytes. Most importantly, these catalysts are not negatively affected by phosphates and are therefore strong candidates for HT-PEMFC cathodes.[4] However, Fe-N-C catalysts have a lower volumetric activity than Pt and suffer from acute performance loss (up to 47 % during the first 100 hours of PEMFC operation).[4-5] Therefore, optimization towards higher electrochemical active site density and higher turnover frequency as well as increased stability is mandatory. Meyer *et al.* suggested novel concepts for improved M-N-C catalysts with a high density of active sites and steered configurations and coordination environments.[6] One approach to achieve a higher active site density is the implementation of carbon nanotubes (CNTs) as carbon support for Fe-N-sites.[7] Recently it was reported by Wu *et al.* that the concept of dual layers of Fe-N_4-C actives sites doubles the turnover frequency of the ORR through an enhancing effect of the sublayer.[8] The degradation of Fe-N-Cs in LT-PEMFC is attributed to active site deactivation in the form of demetallation (agglomeration and dissolution), deactivation and site loss through carbon corrosion.[3-4, 9-10] Li *et al.* reported that pyrrolic coordinated Fe is irreversibly converted to Fe_2O_3 during LT-PEMFC operation (80 °C, 0.2-0.8 V, H_2/O_2) while pyridinic coordinated Fe is stable.[11] Recently, Liu *et al.* revealed a deconvoluted degradation pathway of Fe-N-C from a 60 h operation at high load of 1 A cm^{-2}. They were able to show that initially iron demetallation deactivates the catalysts followed by a carbon corrosion induced deceleration of the ORR.[12] Moreover, the formation of reactive oxygen species (ROS) by a Fenton-like reaction of hydrogen peroxide, formed through the 2-electron ORR pathway, leads to oxidation of the carbon surface and thus corrosion and loss of embedded active sites.[10, 13] Furthermore, it was reported the a oxidized carbon surface leads to weakening of the oxygen binding on active Fe-N_x sites and therefore to a lower ORR turnover frequency.[14] Gu *et al.* proposed the addition of Ti_3C_2-TiO_2 radical scavengers to a Fe-N-C catalyst to receive a more durable ORR catalyst for acidic and alkaline environment.[15] Choi and coworkers used operando spectroscopy to

analyze the potential-dependent degradation of a Fe-N-C catalyst. They proposed stable potential ranges below 0.7 V to avoid degradation in acidic medium.[16]
Fe-N-Cs consist of up to 95 wt% of carbon hosting the active Fe-N_x sites.[9] Therefore, the high stability of the carbon material against corrosion can boost the overall catalyst stability. Most stability studies are based on half-cell level or LT-PEMFC. However, one study shows high stability of a bimetallic FeCu/N-CNT catalyst by so-called phosphate promoted ORR activity.[17] With respect to the used carbon support for Fe-N-C catalysts the higher operating temperatures of HT-PEMFC may accelerate carbon corrosion-induced degradations.[18] Furthermore, the phosphoric acid electrolyte of HT-PEMFC can impact the stability because interactions of the acid with the N-functionalities of the Fe-N-C may occur.[19] Thus, the effect of carbon support in Fe-N-C could play a crucial role in their stability in HT-PEMFCs.

In this study, the stability of four different classes of Fe-N-C catalysts with Fe-N_x sites but with carbon supports with different properties were investigated in HT-PEMFC. Gas diffusion electrodes (GDEs) were fabricated, including a commercial Fe-N-C catalyst (PMF), a catalyst based on Black Pearls® and two Fe-N-Cs based on phosphoric acid activated biomasses. In our previous study, a higher resistance against carbon corrosion for the biomass-based catalysts compared to the Black Pearl-based Fe-N-C were identified from rotating-disc electrode measurements.[20] This was attributed to the presence of P species in these catalyst inhibiting the electron withdrawal from the carbon occurring during carbon oxidation.[20-21] A first performance test of the four GDEs as cathodes in HT-PEMFC showed significant differences in performance mainly attributed to the electrode structure and catalyst layer hydrophilicity.[22] In the presented study, we focused on the analysis of the cell stability over time. This includes voltage monitoring over 90 h at constant load HT-PEMFC operation, investigating the impact of characterization procedures on the cell voltage, and the identification of degradation processes via operando electrochemical methods such as cyclic voltammetry (CV) and electrochemical impedance spectroscopy (EIS) with distribution of relaxation (DRT) analysis as well as post-mortem analysis.

2 Materials and methods

2.1. Fe-N-C catalysts

The catalysts were synthesized via carbon support impregnation with iron(II) acetate and cyanamide, pyrolysis at 900 °C (1 h), acid leaching in sulfuric acid (2 mol L^{-1}) and second pyrolysis at 900 °C. The carbon supports used are oxidized Black Pearls® 2000 (ox-BP, Cabot), phosphoric acid-activated rye straw (aRS_{H3PO4}) and coconut shells ($aCoco_{H3PO4}$). Further details of the catalyst synthesis strategies can be found in our previous studies.[20, 23] A commercial Fe-N-C catalyst PMF-011904 (Pajarito Powder) was also considered as a

benchmark for comparison purposes.[24] The four catalysts used in this study are referred to as Fe-N-C_{PMF}, Fe-N-ox-BP, Fe-N-a$Coco_{H3PO4}$ and Fe-N-aRS_{H3PO4}.

2.2. Fabrication of gas diffusion electrodes and membrane electrode assemblies

GDEs were fabricated by ultrasonic spray-coating (ExactaCoat, Sonotek) on a woven gas diffusion layer (De Nora). The catalyst ink consisted of 1.7 wt% Fe-N-C, 18.7 wt% water, 77.7 wt% 2-propanol and 1.9 wt% of a 60 wt% PTFE dispersion in water (Sigma Aldrich). The catalyst/water/2-propanol suspension was sonicated in an ice bath for 15 min. Next, horn sonication for 15 min with a pulse (30 s on, 10 s off, amplitude of 15 %) was applied, followed by storage of the suspension overnight. PTFE was added and 15 min pulsed horn sonication was applied. The coating was carried out with a 48 kHz nozzle and a flow rate of 0.2 mL min^{-1} and 0.3 mL min^{-1} in the case of the biomass-based Fe-N-C due to sedimentation. 25 cm^2 of GDL was stored on a heating plate at 40 °C for coating. 270 layers were needed to reach loadings in the range of 26-34 μg_{Fe} cm^{-2} which were determined by inductively coupled plasma mass spectrometry (ICP-MS).

For membrane electrode assembly (MEA) preparation, a commercial Celtec® membrane based on phosphoric acid doped polybenzimidazole was stored in 50 wt% H_3PO_4 overnight to ensure similar acid content for all MEAs. The membrane was sandwiched between 5 cm^2 of the fabricated Fe-N-C containing cathode and a commercial Pt/C anode (~1 mg_{Pt} cm^{-2}, De Nora) and two Kapton® frames using hot press for 30 s at 140 °C with 1 kN. Finally, thermal annealing at 120 °C for 30 min was carried out. The final active area was 4.05 cm^2.[22]

2.3. HT-PEMFC

HT-PEMFC performances were evaluated using an Evaluator-C 70316 test station with FuelWork software (FuelCon) equipped with a quickCONNECTfixture (qCF 5/100 HT, balticFuelCells). A cell fixture cF5/100 HT Gr V1.4 with serpentine graphitic flow fields (balticFuelCells) was used. Cell compression of 0.75 MPa was applied during the whole test. After passing the leak test, the cell temperature was increased to 120 °C under nitrogen flow. Then the gases were switched to dry H_2/O_2 with stoichiometry of 1.5/9.5 and the temperature was increased to 160 °C. A constant load of 0.1 A cm^{-2} was applied. After reaching the final operation temperature of 160 °C, the beginning of test (BoT) characterization, constant load test and end of test (EoT) characterization were carried out as described in Table 1. For EIS, CV and linear sweep voltammetry (LSV) measurements, an external potentiostat Modulab2100A (Ametek) equipped with an external booster (12 V/20 A) was used. During the stability test, impedance spectra were recorded every day at the fixed current density of 0.1 A cm^{-2} and after 50 h a CV measurement was performed. After 90 h of operation, an EoT characterization analogue to BoT was carried out followed by a controlled cool down.

Table 1: Overview of HT-PEMFC test parameters.

	Method and gas supply	Parameters
BoT and EoT	Galvanostatic U-I polarization curve H_2/O_2, λ (1.5/9.5)	Start: 0.1 A cm^{-2} Max. current density: 2 A cm^{-2} Minimal voltage: 0.25 V Step size: 0.05 A Holding time per step: 30 s Number of scans: 3
	EIS H_2/O_2, λ (1.5/9.5)	Current densities: 0.03, 0.1, 0.2 A cm^{-2} Amplitude: 0.01 V Frequency: 100 kHz -100 mHz Time between each measurement: 8 min
	CV N_2/H_2 0.1 L min^{-1}	Range: 0.05-1.00 V Scan rate: 100 mV s^{-1} Number of scans: 7
	LSV N_2/H_2 0.3 L min^{-1}	Range: 0.1-0.5 V Scan rate: 2 mV s^{-1}
Stability test	Constant load H_2/O_2, λ (1.5/9.5)	Current density: 0.1 A cm^{-2} Duration min. 90 h

Distribution of relaxation times (DRT) analysis was performed using the data from EIS. Equation (1) displays the relation between the impedance Z, the ohmic resistance R_∞, the polarization resistance R_{pol}, the DRT function g, the relaxation time τ and the frequency f.[25-26]

$$Z(f) = R_\infty + R_{pol}\int_0^\infty \frac{g(\tau)}{1 + i2\pi f\tau}\,d\tau \quad (1)$$

For discrete DRT calculation from the measured impedance data, several logarithmically equally spaced time constants are used using equation (2):

$$Z(f) = R_\infty + R_{\mathrm{pol}}\sum_{k=1}^{N}\frac{g_k}{1 + 2i\pi f\tau_k} \quad (2)$$

The DRT function of the measured spectra is determined using an approach based on the Tikhonov regularization.[27] The regularization level which weights the residual noise against the solution norm is determined by the regularization parameter λ.[28-29] A well-chosen regularization parameter λ is, therefore, necessary to accurately determine the pseudo-continuous DRT function from the discrete impedance dataset. A regularization parameter λ of 10^{-3} was used following Heinzmann's study, as it represents an excellent trade-off between low-residuals, selectivity, and minimal oscillations for hydrogen fuel cells.[27] The Matlab® software *DRTtools* developed by the Ciucci group was used to calculate the DRT function [25-26]. Peaks in the DRT plot were separated and analyzed by applying Voigt deconvolution using Matlab® software DCscript to identify the peak maximum frequency (rate of the process) and calculate the area of each peak under the logarithmic scale (resistance).[30-31]

2.4. Post-mortem analysis of HT-PEMFCs

The iron content of the membrane electrode assemblies at EoT was analyzed by punching out 1 cm^2 of the MEA and analysis by ICP-MS (XSeries2, Thermo Fisher Scientific). Details of sample digestion and ICP-MS calibration are reported in our previous studies.[20, 22-23] Titration for determination of acid content was done for three positions (diameter of 6 mm each). Before titration separation into anode, membrane and cathode and stirring for 30 min in a mixture of 30 mL acetone and 70 mL water was carried out. The solution was analyzed with the autotitrator TitroLine alphaplus (Schott) with an IoLine SI Analytics pH electrode (Schott) and a 0.1 mol L^{-1} sodium hydroxide solution. As the primary standard potassium hydrogen phthalate was used. Transmission electron microscopy (TEM, Zeiss EM 900N) and scanning TEM (Jeol JEM2100 F) with energy dispersive spectroscopy (EDS, Oxford INCA Energy TEM250) was carried out for the cathode catalysts after EoT. For this, the catalyst was dispersed in ethanol and deposited on a 300-mesh copper grid (Plano). Micro-computed tomography (µ-CT) for MEA samples with a diameter of 6 mm was performed on a SkyScan 1172 device (Bruker MicroCT) with an acceleration voltage of 80 kV and a current of 100 µA. Rotation steps of 0.2 °, frame averaging of 4 and random movement of 10 were chosen. The exposure time was 1450 s and the resolution was 1.8-2.1 µm $pixel^{-1}$. The reconstruction was processed using the software NRecon (Bruker) with a greyscale range of 0.0-0.1.

3 Results and discussion

The performances and stability of the commercial Fe-N-C catalyst (Fe-N-C_{PMF}), a carbon black-based Fe-N-C (Fe-N-ox-BP) and two activated biomass-based Fe-N-Cs (Fe-N-a$Coco_{H3PO4}$, Fe-N-aRS_{H3PO4}) were evaluated in HT-PEMFC. A detailed physical analysis of the catalysts and GDEs can be found in our previous study.[22] The Fe-N-C total loadings in GDEs were determined by gravimetric measurements after coating and ranged between 1.7 and 2.8 mg cm^{-2}. The iron loadings from ICP-MS were 32 (Fe-N-C_{PMF}), 34 (Fe-N-ox-BP), 26 and 33 μg_{Fe} cm^{-2} for Fe-N-a$Coco_{H3PO4}$ and Fe-N-aRS_{H3PO4}, respectively.[22]

3.1. Single-cell stability test

The MEAs comprised of the self-fabricated cathode, a commercial Celtec® membrane and a commercial Pt/C anode. For durability evaluation, electrochemical measurements before and after 90 h of operations at 0.1 A cm^{-2} were performed (Figure 1 a)), with polarization curves, EIS, CV and LSV. Moreover, daily EIS measurements were performed, alongside with a CV after 50 h of operation.

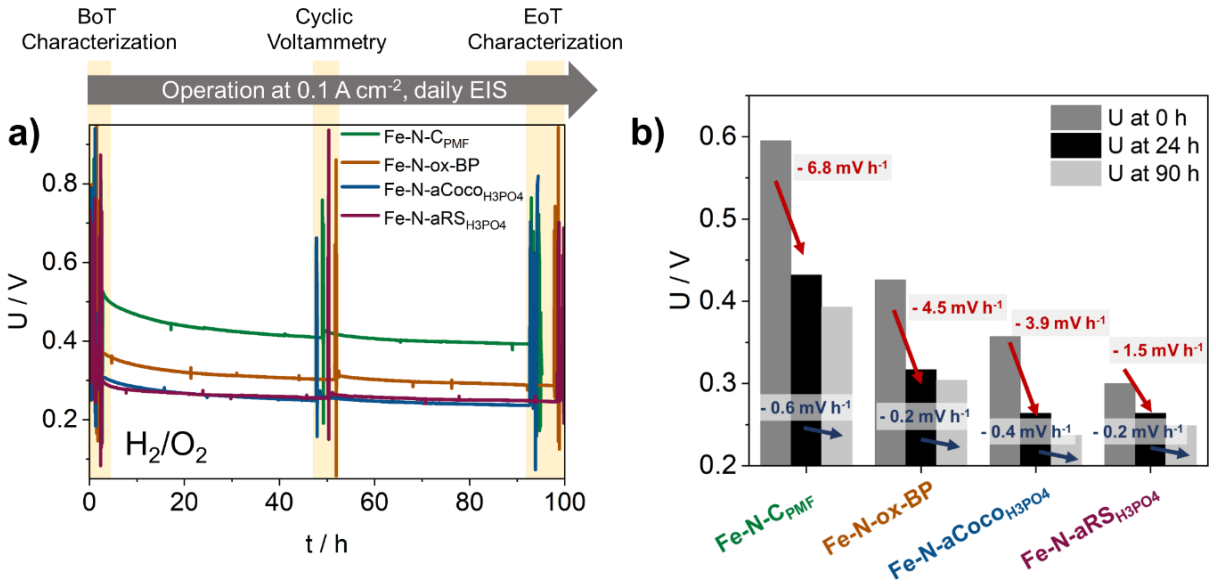

Figure 1: a) Voltage-time plot of HT-PEMFCs operation at 160 °C with dry H_2/O_2 using stoichiometries of 1.5/9.5 and b) voltages at 0 h, 24 h and 90 h of operation at 0.1 A cm^{-2} with indicated loss rates.

Voltages (Figure 1 a) and b)) display differences in the initial values depending on the type of cathode catalyst. While the commercial Fe-N-C_{PMF}-based HT-PEMFC exhibits the highest voltage at 0.1 A cm^{-2} (0.595 V) and therefore highest performance, the biomass-based one has the lowest initial voltages (0.357, 0.300 V). This is attributed to the electrode structure, as similar ORR mass activities of biomass-based and BP-based Fe-N-Cs were determined in previous thin-film analyses.[20, 22] However, independent of starting voltage drastic voltage losses occur within the first 24 h of operation of the Fe-N-C_{PMF}, Fe-N-ox-BP and Fe-N-aCoco$_{H3PO4}$ MEAs in HT-PEMFCs (3.9-6.8 mV h^{-1}, or 26-27 %). (Figure 1 b)). While a voltage loss also occurs for the lowest performing catalyst Fe-N-aRS$_{H3PO4}$ in the first 24 h, this is significantly less severe (1.5 mV h^{-1} or 12 %). In the following 66 h, the voltage losses are significantly dampened (0.2-0.6 mV h^{-1} or 3-8 %) for all MEAs. Thus, the main degradation occurred within the first 24 h of operation regardless of the Fe-N-C catalyst type. This is in agreement with observations by Hu *et al.* for a Black Pearl-based Fe-N-C operated in HT-PEMFC who reported a 28.6 % voltage loss within the first 50 h and merely 5.4 % within a following 350 h, making a longer duration of stability test not mandatory at this point.[32] Several causes have been proposed for voltage decay in the literature. Firstly, the micropores and mesopores may eventually flood with phosphoric acid.[32] Although acid redistribution can enhance the performance in HT-PEMFC, the presence of N-functionalities in Fe-N-C catalysts can cause excessive acid attraction and pore filling inducing strong mass transport limitations.[19] Alternatively, the degradation of the catalyst itself might occur, with deactivation of actives sites by the transformation of unstable Fe-N_x sites into iron oxide clusters between 0.2 and 0.8 V.[11] Moreover, a deactivation can also be induced through the production of

reactive oxygen species attacking both the Fe-N_x sites and the carbon support.[10, 33] The following analysis provides further insights.

To identify the degradation processes within a few hours of operations, it is firstly necessary to determine the impact of the electrochemical analysis on performances. Indeed, for Pt-based catalysts, electrochemical characterizations at BoT can induce MEA degradation through the rapid voltage changes during the recording of polarization curves and CVs.[34] To investigate whether this occurs for Fe-N-C catalysts in HT-PEMFCs, the performances of MEAs from the same batch operated at 0.1 A cm^{-2} with and without BoT characterization were compared (SI Figure S1). For this comparison, the best and the worst-performing MEAs were chosen. The cell voltages are almost identical with and without BoT characterization for both the Fe-N-C_{PMF} and Fe-N-aRS_{H3PO4}, which indicates that the voltage cycling has a negligible influence on the Fe-N-Cs degradation mechanism.

3.2. Electrochemical characterization

The performances at BoT and EoT are firstly analyzed via polarization curves and resulting performance curves from BoT[22] and EoT (Figure 2, zoom SI Figure S2). The initial performance differences are attributed to the higher catalytic activity of Fe-N-C_{PMF} and higher heterogeneities in the electrode structure of MEAs containing biomass-based Fe-N-C.[22] First of all, the changes in open-circuit voltages (OCV) are analyzed. OCV is influenced by hydrogen crossover, mixed potentials as well as catalyst activity.[35] The OCVs decrease in a similar manner for Fe-N-C_{PMF} (-65 mV), Fe-N-ox-BP (-68 mV) and Fe-N-aRS_{H3PO4} (-67 mV), with and a slightly higher decrease of -84 mV for Fe-N-a$Coco_{H3PO4}$. Hydrogen crossover is unlikely to be responsible as a commercial standard membrane was used; besides, the short length of operations (90 h) excluded operations-induced degradations. Therefore, the decrease is attributed to the degradation of the Fe-N-C catalysts with in particular the activity loss of Fe-N_x sites and the oxidation of carbon support resulting in parasitic reactions. The degradation mechanism can involve different processes. Firstly, the most active Fe-N_x sites can become inactive by irreversible transformation to oxides. Secondly, the overall electrochemical active site density reduces via demetallation or aggregation through attack by ROS.

The decrease in power density at 0.1 A cm^{-2} was also analyzed (Figure 2 b)). Analogous to the voltage losses highly comparable performance losses of 23-25 % at 0.1 A cm^{-2} are observed for Fe-N-C_{PMF}, Fe-N-ox-BP and Fe-N-a$Coco_{H3PO4}$ and 15 % in the case of Fe-N-aRS_{H3PO4}. The lower degradation of this catalyst might be attributed to the lowest initial performance. According to our previous studies, the physical properties, ORR activity, site density and higher stability against carbon corrosion of Fe-N-aRS_{H3PO4} are highly comparable to the Fe-N-a$Coco_{H3PO4}$ sample.[20, 22-23] However, voltage and performance show comparable declines for Fe-N-a$Coco_{H3PO4}$ and non-biomass-based Fe-N-Cs. From half-cell measurements

[20], a higher stability of the biomass mass-based Fe-N-Cs against carbon corrosion was observed. Therefore, the carbon supports have a minimal impact on the performance losses within the first hours of operation.

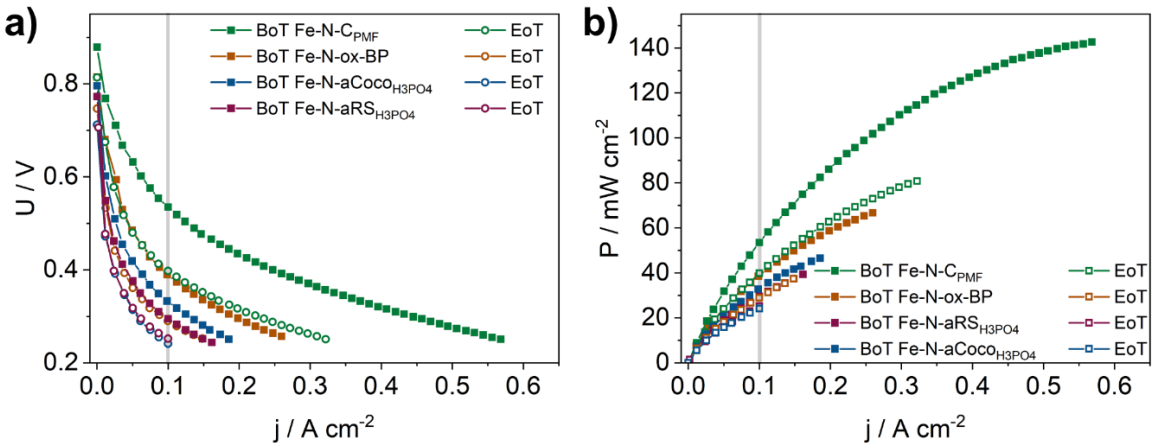

Figure 2: a) U-I polarization curve at BoT[22] and EoT and b) corresponding performance curves recorded at 160 °C, with dry H_2/O_2 using stoichiometries of 1.5/9.5.

To achieve an in-depth analysis of the voltage decay, EIS measurements at 0.1 A cm^{-2} at BoT and EoT were carried out (Figure 3). The differences in Nyquist plots between the four MEAs at BoT are attributed to their different performances and voltages at 0.1 A cm^{-2}. However, in all cases, the overall polarization resistance decreases significantly between BoT and EoT (Figure 3 a)). Bevilacqua *et al.* reported a similar behavior over 120 h of Fe-N-C-based operation with H_2/O_2 at 0.1 A cm^{-2}. However, they observed a simultaneous increase in performance after 120 h and attributed this to decreased ORR and mass transport resistances due to better acid distribution.[36] Comparing the BoT[22] with the EoT, the DRT plots (Figure 3 b)) are dominated by ORR kinetics with minor contributions of proton transport on the anode and cathode and without indication of mass transport limitations in terms of oxygen diffusion which is in accordance to literature.[31] Changes in ORR rate (peak position) and ORR resistance (peak area) between BoT and EoT state can be found in Figure 3 b) and c) (for other rates and resistance of peaks see SI Tables S1-S3). For all MEAs the ORR resistance (R_{ORR}) decreases by 16-28 %. As both the OCV values and performances decreased, an increase in the ORR activity can be excluded. Two possible explanations are proposed (I) Active sites with slow ORR kinetics which contributed to initial performance became inactive leading to decreased ORR resistance. (II) The enhanced oxygen diffusion and adsorption through acid distribution and interaction with N-functionalities but simultaneous deactivation of active sites could reduce the ORR resistance. The ORR rates (Figure 3 c)) also show an increase in rates for Fe-N-ox-BP (56 %), Fe-N-aRS$_{H3PO4}$ (29 %) and Fe-N-aCoco$_{H3PO4}$ (51 %) which would be consistent with the above-mentioned assumption. The ORR rate reduces by 17 % for Fe-N-C$_{PMF}$, indicating a slightly slower ORR process at EoT.

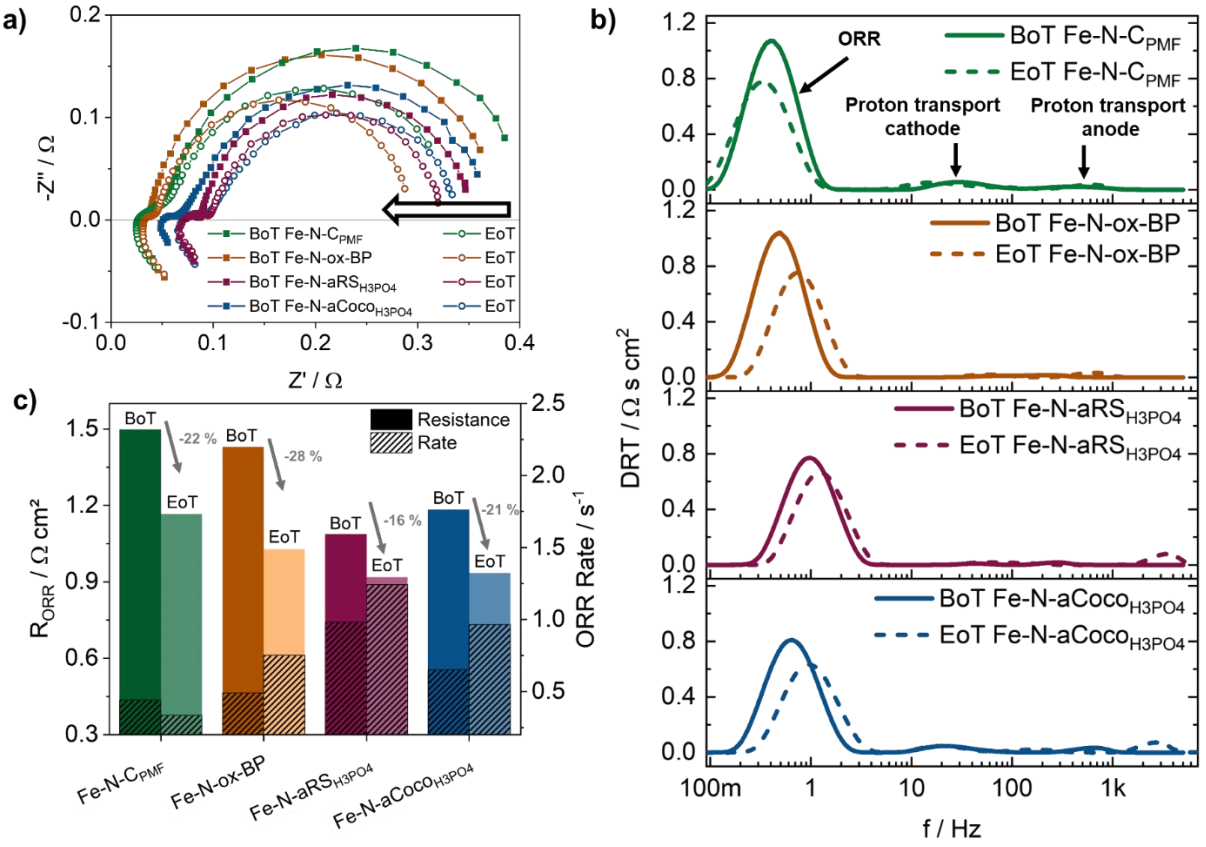

Figure 3: a) Nyquist plots from EIS at 0.1 A cm^{-2} recorded with dry H_2/O_2 with a stoichiometry of 1.5/9.5 at BoT[22] and EoT b) corresponding DRT plots with indicated peaks and c) ORR resistances and ORR rates from DRT analysis.

To further investigate the voltage decay mechanisms for the Fe-N-C$_{PMF}$ and Fe-N-ox-BP, fresh MEAs per each catalyst (denoted as MEA2) from similar GDE batches were used to record EIS hourly for the first 3 hours of operations, followed by daily EIS measurements for the remainder of the 90 h test at 0.1 A cm^{-2}. Nyquist plots and DRT analysis (Figure 4 a, b)) evidence that the most drastic changes take place on the first day of operations with only minor changes from day 2 to day 5, which is consistent with the overall voltage loss (Figure 1). The ORR resistances in Figure 4 c) strongly decrease from 0 h to day 2 for Fe-N-C$_{PMF}$ (17 %) and Fe-N-ox-BP (28 %) with only minor changes from day 2 to day 5 (2 - 8 %). The proton transport rates and resistances of the anode and cathode can be found in SI Tables S4-S6. Our previous work demonstrated that the combination of Pt-catalyst and Fe-N-C$_{PMF}$ prevents the voltage loss within the first hours of operation through synergetic effects e.g. by minimizing ROS formation. Moreover, the activation through acid distribution takes a longer time (up to 120 h) for Fe-N-C/Pt/C hybrid MEAs compared to Pt-based catalysts which were also visible in a decrease in ORR resistance.[37] Thus, the above-mentioned assumption (II), enhanced acid distribution and interaction with N-functionalities but simultaneous deactivation of active sites, might have occurred here. The active sites of the Fe-N-C-based electrodes might be deactivated by the formation of nanoparticles or losses due to the attack by ROS while

simultaneous acid redistribution takes place exposing more accessible active sites. The ORR rates of Fe-N-C_{PMF} and Fe-N-ox-BP are further investigated (Figure 4 c)). While the Fe-N-ox-BP and the biomass-based Fe-N-C MEAs (Figure 3 c) undergo an increase of ORR rates over the whole five days of operation, the Fe-N-C_{PMF} one has an increase in performance in the first hours of operation followed by a decrease from day 2 to day 5. Although the increase of ORR rate for both catalysts might indicate the increase in phosphoric acid diffusion during activation and is consistent with Bevilaqua *et al.*[36] findings, catalyst deactivation is observed. For the Fe-N-C_{PMF} catalysts, the ORR rate evolutions may indicate possible deactivation or transition of active sites into inactive species. This might be attributed to the different catalyst structure of Fe-N-C_{PMF} in terms of porosity and carbon morphology which could lead to different active Fe-N_x site incorporation in micro- or mesopores compared to the other three catalysts (details of physical properties in Ref. [22]). While the Fe-N-C_{PMF} was synthesized via a template-based VariPore™ process[38-39], the other three catalysts were fabricated using a support-based approach[20], so that for the biomass-based Fe-N-C MEAs similar behavior compared to Fe-N-ox-BP MEA is observed. This might furthermore be attributed to the differences in hydrophobicity of the catalysts; while the commercial catalyst has a more hydrophobic character, the Fe-N-C catalysts from the support-based approach are more hydrophilic.

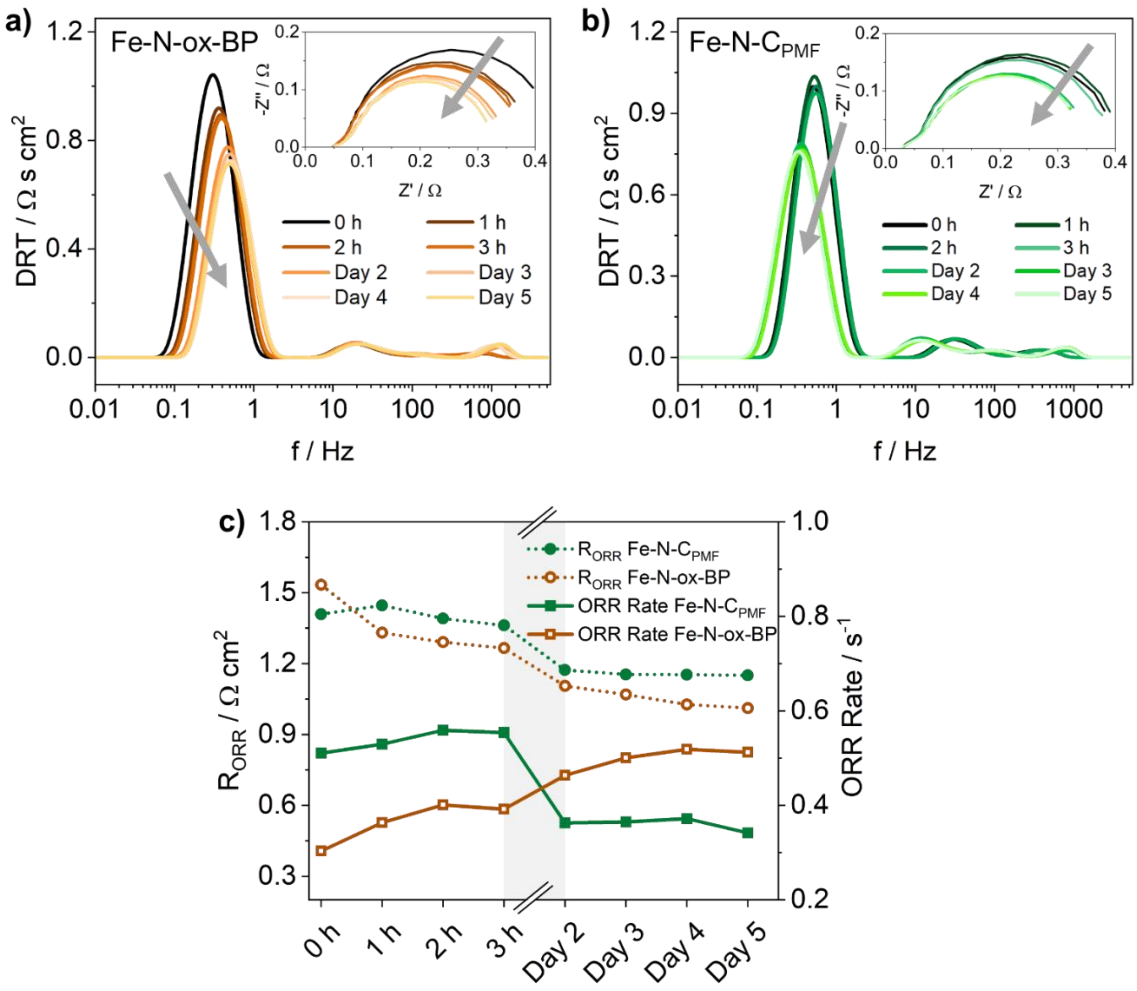

Figure 4: Nyquist plots recorded during operation (insets) and corresponding DRT plots of a) Fe-N-ox-BP, b) Fe-N-C$_{PMF}$ and c) ORR resistance (R$_{ORR}$) and ORR rates.

Lastly, the CVs from BoT[22], after 50 h of operation, and at EoT are analyzed (Figure 5). The CVs of all MEAs have redox peaks in the range of 0.4 - 0.7 V, which become more pronounced after 50 h of operation and without further significant change at EoT. These peaks could be attributed to Fe^{2+}/Fe^{3+} redox transition (~0.76 V[40]) and hydroquinone/quinone redox couple at slightly lower potential indicating oxidized carbon surface.[40-42] The drastic increase of the redox peaks within the first 50 h of operation is consistent with the significant voltage loss (Figure 1). As an increase of Fe^{2+}/Fe^{3+} redox peaks is unlikely to occur, the increased faradaic currents are attributed to the carbon surface oxidation related to hydroquinone/quinone redox peaks. This indicates carbon corrosion and is following the suspected formation of ROS which attack the carbon matrix. Referring to the voltage loss rates in Figure 1 b), the Fe-N-C$_{PMF}$, with its highest loss rate, also has the largest increase (61 %) of anodic current density at 0.65 V after 50 h (Figure 5 a), b)), while the biomass-based catalysts have the lowest loss rates and the lowest increase of current (18 and 19 %). This is in agreement with the half-cell results from our previous studies which revealed a higher resistance to carbon corrosion for the biomass-based Fe-N-Cs.[20] Here, the increased stability was attributed to different electronic

structure of this catalyst class. In more detail, it was proposed that higher ratios of nitrogen functionalities and especially the presence of phosphor species stabilize the carbon network against corrosion by inhibiting electron withdrawal from carbon.

While carbon corrosion impacts each catalyst differently, this is unlikely to be the main drive of the voltage loss, as similar voltage decays occur for all MEAs. Instead, the deactivation of active sites (e.g. transformation or attack of carbon by close to the active site) could be the main driving force. While the ROS formation can indirectly be verified through the increase of hydroquinone/quinone redox peaks, the deactivation of active sites cannot directly be concluded from the CV as the hydroquinone/quinone species narrowly overlap with the Fe^{2+}/Fe^{3+} redox peak. Similar redox peaks and increases of faradaic current were observed in the LT-PEMFC study by Snitkoff *et al.* for Fe-N-C_{PMF} catalyst. There, the advanced Fourier transform alternating current voltammetry (FTacV) in combination with CV and EIS was applied and with that an overall loss in electrochemical active site density was identified.[40] This agrees well with the observations and assumption in the present HT-PEMFC study, that the deactivation of active sites e.g. by the formation of inactive nanoparticles or by complete loss through attack by ROS is responsible for the voltage decay.

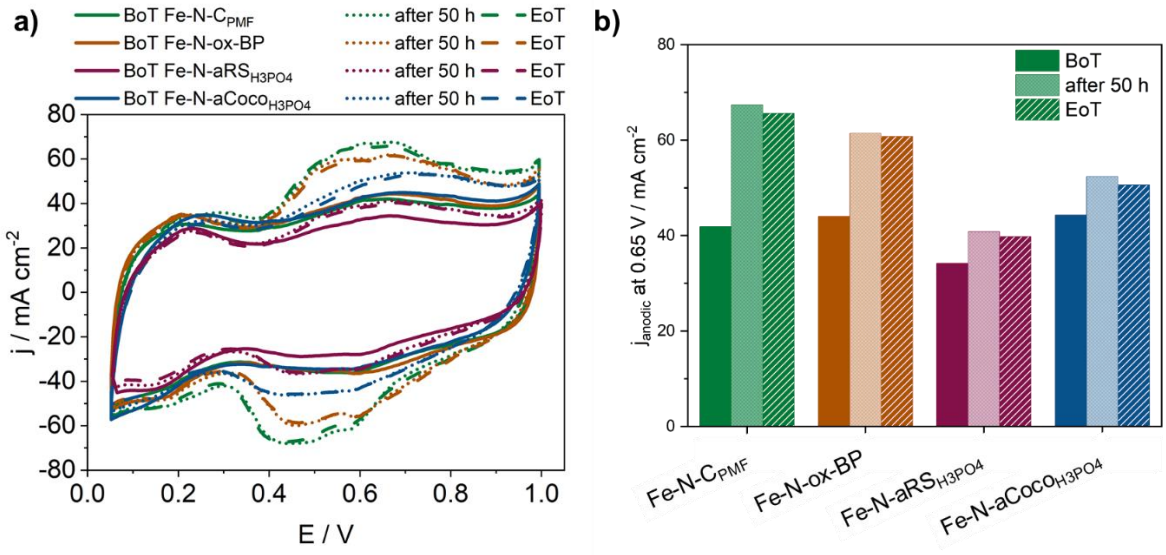

Figure 5: a) CVs of cathodes recorded at BoT, after 50 h of operation and EoT with a scan rate of 0.1 V s^{-1} and H_2/N_2 flow rate of 0.1 L min^{-1} and b) corresponding anodic current densities determined at 0.65 V.

3.3. Post-mortem analysis

For physical identification of degradation processes a post-mortem analysis was carried out. Morphological investigation of the EoT MEA and catalyst layer by µ-CT displayed no drastically changes and differences between the EoT MEAs (SI Figure S2). Titration of the MEAs after the test (Table 2) unveils highly comparable acid contents in range with a commercial Pt-based Celtec®-P1200 MEA (22 mg cm^{-2}). As no significant differences between the MEAs is

observed, this seems not to impact the degradation within the first 90 h of operation. Further on, the iron content of the EoT MEAs was determined by ICP-MS and compared with the values of the pristine GDEs (Table 2). For the Fe-N-C_{PMF} and Fe-N-ox-BP ones, the Fe content at EoT is lower than for the pristine GDEs. This could indicate Fe dissolution and discharge of the cell through the water-acid mixture. For the biomass-based HT-PEMFC, higher Fe contents were found at EoT compared to pristine GDEs, which can be assigned to inherent heterogeneities previously reported for these materials.[22] However, only one measurement was possible due to limited sample availability for ICP-MS. Therefore, no mean value and standard deviation was determined and the increase and decrease of Fe content could be in the error range.

Table 2: Acid contents of MEAs determined by titration and Fe contents of pristine GDE and MEA at EoT from ICP-MS.

	Acid content at EoT / mg cm^{-2}	Fe content / µg cm^{-2}	
		Pristine GDE	MEA at EoT
Fe-N-C_{PMF}	25.5 ± 0.8	32	28
Fe-N-ox-BP	26.5 ± 0.6	34	27
Fe-N-aRS_{H3PO4}	24.7 ± 0.2	33	34
Fe-N-$aCoco_{H3PO4}$	24.1 ± 1.2	26	30

Further investigations of the catalyst morphology were achieved by detaching the Fe-N-C-containing cathodic catalyst layer from the EoT MEA and characterizing its catalysts with TEM and STEM/EDS (Figure 6). For the Fe-N-C_{PMF}, the TEM images reveal the formation of Fe particle (Figure 6 a)) indicating iron dissolution and redeposition or agglomeration of small nanoclusters (STEM/EDS of fresh particle free Fe-N-C_{PMF} in SI Fig. S3). For the other three catalysts (Figure 6 b-d)) no Fe nanoparticles could be identified. It has to be mentioned that TEM only reflects a small part of the sample so that particle formation in case of the other catalysts cannot be excluded completely. For the biomass-based catalysts, large PTFE binder agglomerates are observed (Figure 6 d)) which might be caused by catalyst layer heterogeneities due to inferior interaction between the hydrophobic binder and the hydrophilic Fe-N-C catalysts. The post-mortem analyses also indicate direct degradation of active sites through Fe loss and the formation of nanoparticles.

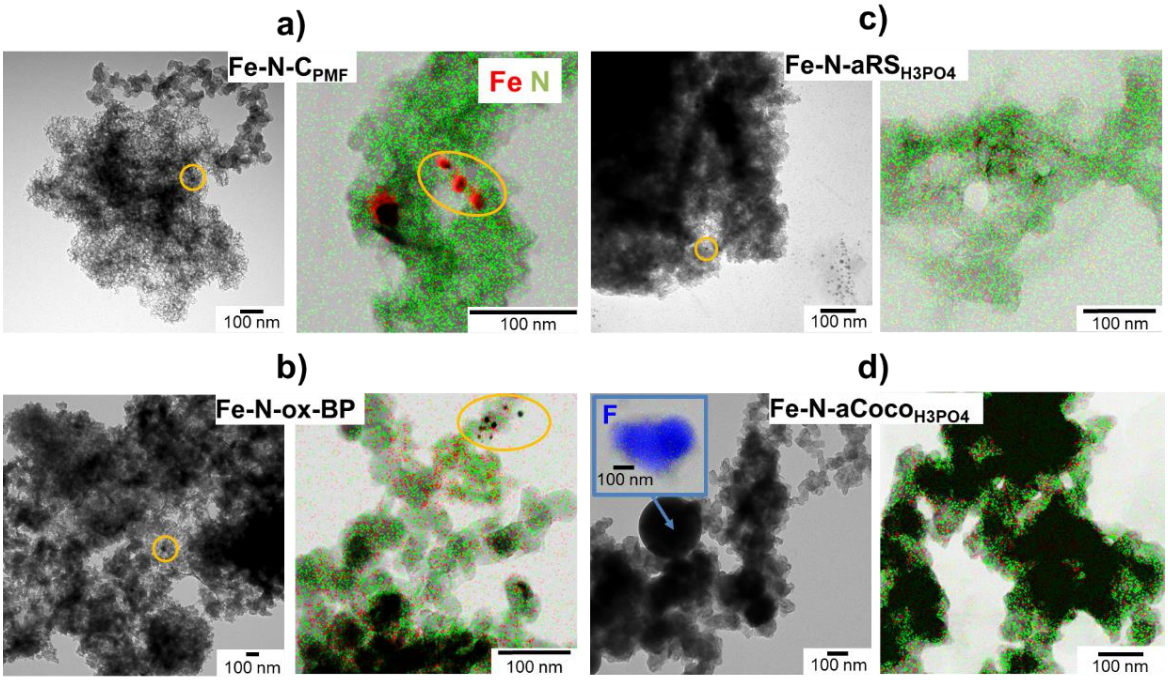

Figure 6: TEM images and Fe, N elemental mapping from STEM/EDS of cathode catalysts at EoT for a) Fe-N-C_{PMF}, b) Fe-N-aRS_{H3PO4}, c) Fe-N-ox-BP and d) Fe-N-$aCoco_{H3PO4}$.

4 Conclusion

Four different classes of Fe-N-C cathode catalysts were used to investigate the stability of Fe-N-C-based cathodes in HT-PEMFCs. Regardless of the Fe-N-C catalyst carbon support, a drastic voltage loss (up to 27 %) occurs after 24 h of operation. This was attributed to the deactivation and loss of active Fe-N_x sites. Moreover, carbon corrosion was identified. Although it had a lower impact on the voltage loss, it indicated the formation of reactive oxygen species during cell operation with different level of severities based on the type of carbon support used. These ROS induced loss of active sites and transformation of active sites into metal clusters or metal oxides might be the main drive for the active site loss in this study. In contrast to LT-PEMFC, besides the deactivation, a slight activation behavior through better phosphoric acid electrolyte distribution was evidenced using DRT analysis after a day of operation. Nevertheless, this improvement was overshadowed by the subsequent deactivation of active sites. In the future, the active sites will have to be modified towards better selectivity to prevent ROS formation, e.g. via the implementation of other metals like Sn or dual atom sites. Moreover, the fabrication of Fe-N-C-based gas diffusion electrode for HT-PEMFC must be optimized. Overall, this study paves the way for further high-performance Fe-N-C catalysts in HT-PEMFCs while proposing an electrochemically-driven characterization framework.

Acknowledgements

This work is part of the funding 03ETB016A of the Federal Ministry for Economic Affairs and Climate Action based on the basis of a decision by the German Bundestag. The authors would like to thank Shirin Karaman and Nina Bengen (both DLR) for titration and ICP-MS measurements. The authors acknowledge the Electron and Light Microscopy Service Unit of the School of Mathematics and Science of the Carl von Ossietzky University for the use of the imaging facilities. Y.N, Q.M and C.Z. acknowledge the Australian Research Council support for this work [LP200100255, DP220103294, IC200100023].

References

[1] R. E. Rosli, A. B. Sulong, W. R. W. Daud, M. A. Zulkifley, T. Husaini, M. I. Rosli, E. H. Majlan, M. A. Haque, *Int. J. Hydrogen Energy* **2017**, *42*, 9293.10.1016/j.ijhydene.2016.06.211

[2] K. H. Lim, A. S. Lee, V. Atanasov, J. Kerres, E. J. Park, S. Adhikari, S. Maurya, L. D. Manriquez, J. Jung, C. Fujimoto, I. Matanovic, J. Jankovic, Z. D. Hu, H. F. Jia, Y. S. Kim, *Nat Energy* **2022**, *7*, 248.10.1038/s41560-021-00971-x

[3] N. Seselj, S. M. Alfaro, E. Bompolaki, L. N. Cleemann, T. Torres, K. Azizi, *Advanced Materials* **2023**, *n/a*, 2302207.https://doi.org/10.1002/adma.202302207

[4] Q. Meyer, C. Yang, Y. Cheng, C. Zhao, *Electrochemical Energy Reviews* **2023**, *6*, 1.10.1007/s41918-023-00180-y

[5] F. Jaouen, D. Jones, N. Coutard, V. Artero, P. Strasser, A. Kucernak, *Johnson Matthey Technol. Rev.* **2018**, *62*, 231.10.1595/205651318x696828

[6] Q. Meyer, C. J. Yang, Y. Cheng, C. Zhao, *Electrochem Energy R* **2023**, *6*.ARTN 16, 10.1007/s41918-023-00180-y

[7] Y. Cheng, J. Y. Zhang, X. Wu, C. J. Tang, S. Z. Yang, P. P. Su, L. Thomsen, F. P. Zhao, S. F. Lu, J. Liu, S. P. Jiang, *Nano Energy* **2021**, *80*.ARTN 105534, 10.1016/j.nanoen.2020.105534

[8] X. Wu, Q. C. Wang, S. Z. Yang, J. Y. Zhang, Y. Cheng, H. L. Tang, L. Ma, X. B. Min, C. J. Tang, S. P. Jiang, F. X. Wu, Y. P. Lei, S. Ciampic, S. Y. Wang, L. M. Dai, *Energy & Environmental Science* **2022**, *15*, 1183.10.1039/d1ee03311e

[9] U. Martinez, S. Komini Babu, E. F. Holby, H. T. Chung, X. Yin, P. Zelenay, *Adv. Mater.* **2019**, *31*, 1806545.10.1002/adma.201806545

[10] K. Kumar, L. Dubau, M. Mermoux, J. Li, A. Zitolo, J. Nelayah, F. Jaouen, F. Maillard, *Angew. Chem., Int. Ed. Engl.* **2020**, *59*, 3235.10.1002/anie.201912451

[11] J. Li, M. T. Sougrati, A. Zitolo, J. M. Ablett, I. C. Oğuz, T. Mineva, I. Matanovic, P. Atanassov, Y. Huang, I. Zenyuk, A. Di Cicco, K. Kumar, L. Dubau, F. Maillard, G. Dražić, F. Jaouen, *Nat. Catal.* **2020**, *4*, 10.10.1038/s41929-020-00545-2

[12] S. Y. Liu, Q. Meyer, C. Jia, S. H. Wang, C. L. Rong, Y. Nie, C. Zhao, *Energy & Environmental Science* **2023**.10.1039/d3ee01166f

[13] G. Bae, S. H. Han, H. S. Oh, C. H. Choi, *Angew Chem Int Edit* **2023**.10.1002/anie.202219227

[14] C. H. Choi, H.-K. Lim, M. W. Chung, G. Chon, N. Ranjbar Sahraie, A. Altin, M.-T. Sougrati, L. Stievano, H. S. Oh, E. S. Park, F. Luo, P. Strasser, G. Dražić, K. J. J. Mayrhofer, H. Kim, F. Jaouen, *Energy & Environmental Science* **2018**, *11*, 3176.10.1039/C8EE01855C

[15] W. L. Gu, J. B. Xu, J. Sun, T. S. Zhao, *International Journal of Hydrogen Energy* **2023**, *48*, 5323.10.1016/j.ijhydene.2022.11.048

[16] C. H. Choi, C. Baldizzone, J. P. Grote, A. K. Schuppert, F. Jaouen, K. J. Mayrhofer, *Angewandte Chemie* **2015**, *54*, 12753.10.1002/anie.201504903

[17] Y. Cheng, M. E. Wang, S. F. Lu, C. J. Tang, X. Wu, J. P. Veder, B. Johannessen, L. Thomsen, J. Zhang, S. Z. Yang, S. Y. Wang, S. P. Jiang, *Appl Catal B-Environ* **2021**, *284*.ARTN 119717, 10.1016/j.apcatb.2020.119717
[18] V. Goellner, C. Baldizzone, A. Schuppert, M. T. Sougrati, K. Mayrhofer, F. Jaouen, *Phys. Chem. Chem. Phys.* **2014**, *16*, 18454.10.1039/c4cp02882a
[19] N. Pimperl, N. Bevilacqua, M. A. Schmid, P. A. Loichet Torres, H. A. El-Sayed, R. Zeis, K. P. Zeyer, *J. Power Sources* **2021**, *507*, 229971.10.1016/j.jpowsour.2021.229971
[20] J. Müller-Hülstede, D. Schonvogel, H. Schmies, P. Wagner, A. Dyck, M. Wark, *ACS Appl. Energy Mater.* **2021**, *4*, 6912.10.1021/acsaem.1c01018
[21] D.-W. Wang, D. Su, *Energy Environ. Sci.* **2014**, *7*, 576.10.1039/c3ee43463j
[22] J. Müller-Hülstede, T. Zierdt, H. Schmies, D. Schonvogel, Q. Meyer, C. Zhao, P. Wagner, M. Wark, *J Power Sources* **2022**, *537*, 231529.10.1016/j.jpowsour.2022.231529
[23] J. Hülstede, D. Schonvogel, H. Schmies, P. Wagner, F. Schröter, A. Dyck, M. Wark, *Materials (Basel, Switz.)* **2020**, *14*, 45.10.3390/ma14010045
[24] M. Primbs, Y. Sun, A. Roy, D. Malko, A. Mehmood, M.-T. Sougrati, P.-Y. Blanchard, G. Granozzi, T. Kosmala, G. Daniel, P. Atanassov, J. Sharman, C. Durante, A. Kucernak, D. Jones, F. Jaouen, P. Strasser, *Energy Environ. Sci.* **2020**, *13*, 2480.10.1039/d0ee01013h
[25] F. Ciucci, C. Chen, *Electrochim. Acta* **2015**, *167*, 439.10.1016/j.electacta.2015.03.123
[26] T. H. Wan, M. Saccoccio, C. Chen, F. Ciucci, *Electrochim. Acta* **2015**, *184*, 483.10.1016/j.electacta.2015.09.097
[27] M. Heinzmann, A. Weber, E. Ivers-Tiffée, *J Power Sources* **2018**, *402*, 24.10.1016/j.jpowsour.2018.09.004
[28] A. N. Tikhonov, V. J. Arsenin, V. I. A. k. Arsenin, V. Y. Arsenin, *Solutions of ill-posed problems*, Vh Winston, **1977**.
[29] J. Chamorro-Servent, R. Dubois, Y. Coudière, *Frontiers in Physiology* **2019**, *10*.10.3389/fphys.2019.00273
[30] Maxim (2022). Peak fitting to either Voigt or LogNormal line shapes. (https://www.mathworks.com/matlabcentral/fileexchange/52321-peak-fitting-to-either-voigt-or-lognormal-line-shapes), MATLAB Central File Exchange. Retrieved January 19, 2022.
[31] Q. Meyer, S. Y. Liu, Y. B. Li, C. A. Zhao, *J Power Sources* **2022**, *533*.10.1016/j.jpowsour.2022.231058
[32] Y. Hu, J. O. Jensen, C. Pan, L. N. Cleemann, I. Shypunov, Q. Li, *Appl. Catal., B* **2018**, *234*, 357.10.1016/j.apcatb.2018.03.056
[33] G. Bae, M. W. Chung, S. G. Ji, F. Jaouen, C. H. Choi, *ACS Catal.* **2020**, *10*, 8485.10.1021/acscatal.0c00948
[34] D. Schonvogel, M. Rastedt, P. Wagner, M. Wark, A. Dyck, *Fuel Cells* **2016**, *16*, 480.10.1002/fuce.201500160
[35] P. Mardle, I. Cerri, T. Suzuki, A. El-kharouf, *Catalysts (Basel, Switz.)* **2021**, *11*, 965.10.3390/catal11080965
[36] N. Bevilacqua, T. Asset, M. A. Schmid, H. Markötter, I. Manke, P. Atanassov, R. Zeis, *J. Power Sources Advances* **2021**, *7*, 100042.10.1016/j.powera.2020.100042
[37] J. Müller-Hülstede, L. M. Uhlig, H. Schmies, D. Schonvogel, Q. Meyer, Y. Nie, C. Zhao, J. Vidakovic, P. Wagner, *ChemSusChem* **2023**, *16*, e202202046.10.1002/cssc.202202046
[38] F. D. Speck, J. H. Kim, G. Bae, S. H. Joo, K. J. J. Mayrhofer, C. H. Choi, S. Cherevko, *JACS Au* **2021**, *1*, 1086.10.1021/jacsau.1c00121
[39] H. Kishi, T. Sakamoto, K. Asazawa, S. Yamaguchi, T. Kato, B. Zulevi, A. Serov, K. Artyushkova, P. Atanassov, D. Matsumura, K. Tamura, Y. Nishihata, H. Tanaka, *Nanomaterials (Basel, Switz.)* **2018**, *8*, 965.10.3390/nano8120965
[40] R. Z. Snitkoff-Sol, A. Friedman, H. C. Honig, Y. Yurko, A. Kozhushner, M. J. Zachman, P. Zelenay, A. M. Bond, L. Elbaz, *Nat Catal* **2022**, *5*, 163.10.1038/s41929-022-00748-9

[41] A. Zana, J. Speder, N. E. A. Reeler, T. Vosch, M. Arenz, *Electrochim. Acta* **2013**, *114*, 455.10.1016/j.electacta.2013.10.097
[42] A. Alsudairi, J. Li, N. Ramaswamy, S. Mukerjee, K. M. Abraham, Q. Jia, *J. Phys. Chem. Lett.* **2017**, *8*, 2881.10.1021/acs.jpclett.7b01126